PNAS RESEARCH ARTICLE | ENGINEERING

# Ultrasound-responsive liposomes: A mechanistic framework to decode the effects of acoustic parameters

Ignasi Simon[a,b], Rebecca F. A. van den Elshout[a], Gandhika K. Wardhana[b], Masoumeh Aqamolaei[b], Isabella S. T. de Jonge[a], Remco Hartkamp[c], Riccardo Alessandri[d], Tiago L. Costa[b,1], and Alina Y. Rwei[a,1]

Affiliations are included on p. 9.

Edited by Chengzhi Shi, University of Michigan, Atlanta, GA; received December 6, 2025; accepted February 27, 2026 by Editorial Board Member Catherine J. Murphy

**Ultrasound offers a noninvasive, clinically relevant means to achieve precise spatiotemporal control of cargo release from ultrasound-responsive drug delivery systems within deep tissues. This approach enables targeted delivery of therapeutic agents, enhancing efficacy while minimizing systemic toxicity. While previous studies show that release from ultrasound-responsive liposomes depends on acoustic parameters, the underlying mechanisms remain unclear. A deeper mechanistic understanding is essential to achieve precision over release and maximize therapeutic outcomes. To address this, we propose a sonoporation-based framework to describe release dynamics across varying frequencies, pressures, duty cycles, and pulse repetition frequencies for ultrasound-responsive poly(ethylene glycol)-functionalized liposomes. Using computational simulations validated by empirical results, our framework identifies a critical pressure threshold for release onset and demonstrates how the time spent above this threshold, modulated by acoustic parameters, governs release efficiency. To elucidate these effects, custom-built ultrasound transducers with different resonance frequencies were fabricated and characterized to ensure precise sample alignment, minimize acoustic distortion, and maintain a controlled focal-volume-to-sample-volume ratio across different frequencies. COMSOL simulations indicated that oscillatory acoustic pressure plays a more dominant role than acoustic radiation force, while coarse-grained molecular dynamics simulations captured pressure-dependent pore formation dynamics within the lipid bilayer. Together, our experiments and simulations highlight mechanical effects—particularly oscillatory acoustic pressure—as the primary driver of sonoporation-facilitated release. Finally, we discuss how optimizing acoustic parameters through this mechanistic framework could facilitate safe and effective clinical translation by considering tissue safety and ultrasound transducer design.**

ultrasound | acoustic pressure | sonoporation | liposomes | drug delivery

## Significance

Ultrasound can trigger the release of drugs from ultrasound-responsive liposomes at precise locations within the body, enabling on-target delivery of therapeutics while minimizing side effects. While multiple factors influence the clinical translation of this technology, a key scientific barrier is the limited mechanistic understanding of how acoustic parameters such as frequency, pressure, and duty cycle govern release. We propose a mechanistic framework in which ultrasound parameters modulate sonoporation-driven release by accounting for the temporal and spatial distribution of ultrasound waves. This mechanistic understanding can guide the selection of acoustic conditions and the design of ultrasonic transducers for safer and more effective clinical translation of ultrasound-responsive liposomes.

The overarching goal of nanomedicine in drug delivery is to enhance the bioavailability of active pharmaceutical ingredients (API) at their site of action while minimizing systemic exposure (1, 2). Nanoparticles can prolong systemic circulation, improve the stability and solubility of therapeutic cargos, and facilitate their transport across biological barriers, thereby improving overall therapeutic efficacy and safety (3). While conventional nanomedicines primarily rely on passive accumulation via the enhanced permeability and retention effect, in the context of ultrasound drug delivery, microbubble-assisted opening of endothelial or blood–brain barriers has been used to further facilitate nanoparticle transport (4). Liposomes are among the most extensively studied nanocarriers due to their clinically validated biocompatibility, ability to encapsulate both hydrophilic and hydrophobic compounds, and tunable physicochemical properties (5, 6). However, current clinically approved liposomal formulations, such as Doxil®, suffer from suboptimal on-target API release, hindering their therapeutic effectiveness (7).

To overcome these limitations, stimuli-responsive liposomes have been engineered to release the therapeutic cargo in response to endogenous and external stimuli (8), including clinically translated formulations such as ThermoDox® and THE001, which were designed with thermosensitive lipids and evaluated under hyperthermia (9, 10). Among the variety of triggering technologies, ultrasound has emerged as a clinically validated and noninvasive modality for spatiotemporally controlled release (11). Ultrasound–pressure waves with frequencies above the 20 kHz human hearing limit - combines deep tissue penetration with an attenuation of ~0.7 dB/cm/MHz in soft tissues (12), precise focusing with spatial resolutions in the millimeter to submillimeter range, and clinically validated safety profiles, enabling therapeutic uses such as neuromodulation (13), histotripsy (14), thermal tissue

Author contributions: I.S., R.F.A.v.d.E., G.K.W., M.A., R.H., R.A., T.L.C., and A.Y.R. designed research; I.S., R.F.A.v.d.E., and I.S.T.d.J. performed research; I.S., R.F.A.v.d.E., T.L.C., and A.Y.R. analyzed data; and I.S., T.L.C., and A.Y.R. wrote the paper.

The authors declare no competing interest.

This article is a PNAS Direct Submission. C.S. is a guest editor invited by the Editorial Board.



[1]To whom correspondence may be addressed. Email: T.M.L.daCosta@tudelft.nl or A.Y.Rwei@tudelft.nl.

This article contains supporting information online at https://www.pnas.org/lookup/suppl/doi:10.1073/pnas.2535429123/-/DCSupplemental.

Published March 25, 2026.

ablation (15), blood–brain barrier opening (16), sonothrombolysis (17), chronic pain management (18), and ultrasound-triggered drug delivery (19, 20). Among ultrasound-responsive drug nanocarriers, liposomes capable of releasing their cargo upon ultrasound insonation without requiring perfluorocarbons, as employed in phase-change nanodroplets, are referred to here as ultrasound-responsive liposomes. These systems offer promising stability, biocompatibility, and encapsulation efficiency across a wide range of APIs, supporting their potential for clinical translation (21–23).

While in theory purposed for chemical synthesis (24), low-frequency tip sonicators (20 to 50 kHz) have also been utilized to examine drug release kinetics from ultrasound-responsive liposomes (22, 25, 26), as well as the role of polyethylene glycol (PEG)-lipid conjugates (27), lipid headgroup composition (28), and the effect of targeting moieties in modulating release efficiency (29, 30). These studies have demonstrated how formulation optimization can enhance ultrasound-triggered cargo release from liposomes, as well as proof of concept both in vitro and in vivo (31, 32). However, the low frequency and aperture of tip sonicators impose a shallow near-field region, which prevents well-defined focusing in deep tissue. Furthermore, commercially available tip sonicators have limited reconfigurability of pulse repetition frequency (PRF) and duty cycle (DC). As a result, they offer limited mechanistic insights and are poorly suited for clinical translation.

More recent in vivo studies using commercial transducers with defined beam profiles have underscored the translational potential of ultrasound-triggered release (33–38). Yet, these transducers were largely repurposed from other therapeutic applications and not specifically engineered or operated based on fundamental knowledge of the optimal acoustic conditions required for effective cargo release. This reliance on repurposed transducers has constrained the range of ultrasound parameters explored, revealing a critical gap in the mechanistic understanding of the effect of acoustic parameters. Addressing this limitation requires a systematic investigation of acoustic parameters and a deeper mechanistic understanding of their influence on release from ultrasound-triggered liposomes. Together, these insights will enable the rational design of ultrasound transducers tailored to ultrasound-triggered release from liposomes for optimal therapeutic outcomes.

While several studies have explored the role of acoustic pressure in ultrasound-triggered liposomal release, the effects of other key parameters, such as frequency, DC, or PRF, have been far less systematically investigated (39–41). In addition, reported trends remain inconsistent, reflecting the incomplete understanding of how acoustic parameters govern release. For example, a study showed no apparent frequency dependence of release rate, though the focal region only partially covered the sample, and exposure volumes differed between frequencies (40). In contrast, others observed higher releases at lower frequencies for a given pressure (39) and greater release using 20 kHz tip sonicators than MHz-range transducers, but did not account for the distinct beam profile of each transducer (41). Collectively, variations in transducer type, beam geometry, and unaccounted acoustic field distortions impede the mechanistic interpretation of ultrasound–lipid bilayer interactions and the effect of acoustic parameters. This is because the volume of liposomes affected by ultrasound depends strongly on the beam profile, which varies from complex interference patterns near the transducer to a well-defined focal spot at the near-/far-field boundary. In addition, distortions in the beam caused by measurement setups introduce further uncertainty to the volume of liposomes that is affected by the ultrasound waves. Overall, a mechanistic understanding of ultrasound-triggered liposomal release demands a characterization setup where the beam geometry and acoustic field distortions are precisely determined.

To address this gap, and inspired by recent studies demonstrating the importance of understanding ultrasound–tissue interactions in other ultrasound therapeutic modalities (42–45), we propose a sonoporation-based framework—where sonoporation refers to ultrasound-induced transient pore formation in the lipid bilayer of liposomes, rather than the microbubble-mediated sonoporation commonly discussed in the literature (4)—to elucidate how acoustic parameters govern release. In this framework, release occurs when the acoustic pressure exceeds a critical threshold that induces transient pore formation within the lipid bilayer. Consequently, the extent of release is determined by the spatiotemporal distribution of pressures exceeding this threshold, which in turn depends on the specific acoustic parameters. To experimentally validate this framework, we evaluated the effects of frequency, pressure, DC, and PRF on cargo release using custom-fabricated ultrasound transducers operating at 0.275, 0.725, and 1 MHz. These frequencies were chosen because, in a clinical context, they offer an optimal balance between penetration depth through bone and soft tissue and the practical dimensions of the transducer, both typically on the order of several centimeters. These transducers were characterized by their spatial beam profiles, frequency responses, pressure-voltage transmit sensitivity, and focal volumes. Custom-designed polydimethylsiloxane (PDMS) cuvettes and experimental beam mapping ensured control over the focal-volume-to-sample-volume ratio and minimized acoustic distortion. In parallel, 3D-printed holders provided precise alignment of the cuvettes within the ultrasound focal volume. COMSOL modeling suggested oscillatory acoustic pressure to dominate over acoustic radiation force, while complementary coarse-grained molecular dynamics simulations elucidated pressure-dependent pore formation in lipid bilayers. Finally, this work discusses how the identified optimal acoustic parameters and proposed mechanistic framework could guide safer and more effective clinical translation of ultrasound-responsive liposomes by considering ultrasound transducer design and ultrasound parameters-related tissue safety constraints.

## Results

**Characterization of Ultrasound-Responsive Liposomes and Custom Ultrasound Transducer Setup.** Ultrasound-responsive liposomes composed of 35% 1,2-dioleoyl-sn-glycero-3-phosphocholine (DOPC), 35% 1,2-distearoyl-sn-glycero-3-phosphocholine (DLPC), 22.5% cholesterol, and 7.5% 1,2-distearoyl-sn-glycero-3-phosphoethanolamine-N-[methoxy(polyethylene glycol)-2000] (DSPE-PEG2000) were synthesized. This formulation was chosen for its ultrasound-triggered release efficiency (Fig. 1 *B*–*D*) and its structural and cargo entrapment stability (*SI Appendix*, Fig. S1 *C* and *F*). The synthesized liposomes had an average size of 115 ± 1 nm and a polydispersity index (PDI) of 0.04 ± 0.01 as confirmed by dynamic light scattering (*SI Appendix*, Fig. S1*A*), and a zeta potential of –6.1 ± 0.4 mV (*SI Appendix*, Fig. S1*B*). Cryo-TEM confirmed liposomal morphology (*SI Appendix*, Fig. S1*E*). Structural stability was confirmed in storage conditions (4 °C) with no change in size or PDI after 10 d (*SI Appendix*, Fig. S1 *C* and *D*). Cargo encapsulation was stable at body temperature (37 °C), with less than 1% release after 2 h (*SI Appendix*, Fig. S1*F*). UV-Vis and fluorescence spectroscopy confirmed self-quenched calcein encapsulation, as evidenced by its characteristic absorption peak at roughly 495 nm (*SI Appendix*, Fig. S1*G*) and reduced emission peak at around 517 nm (*SI Appendix*, Fig. S1*H*).

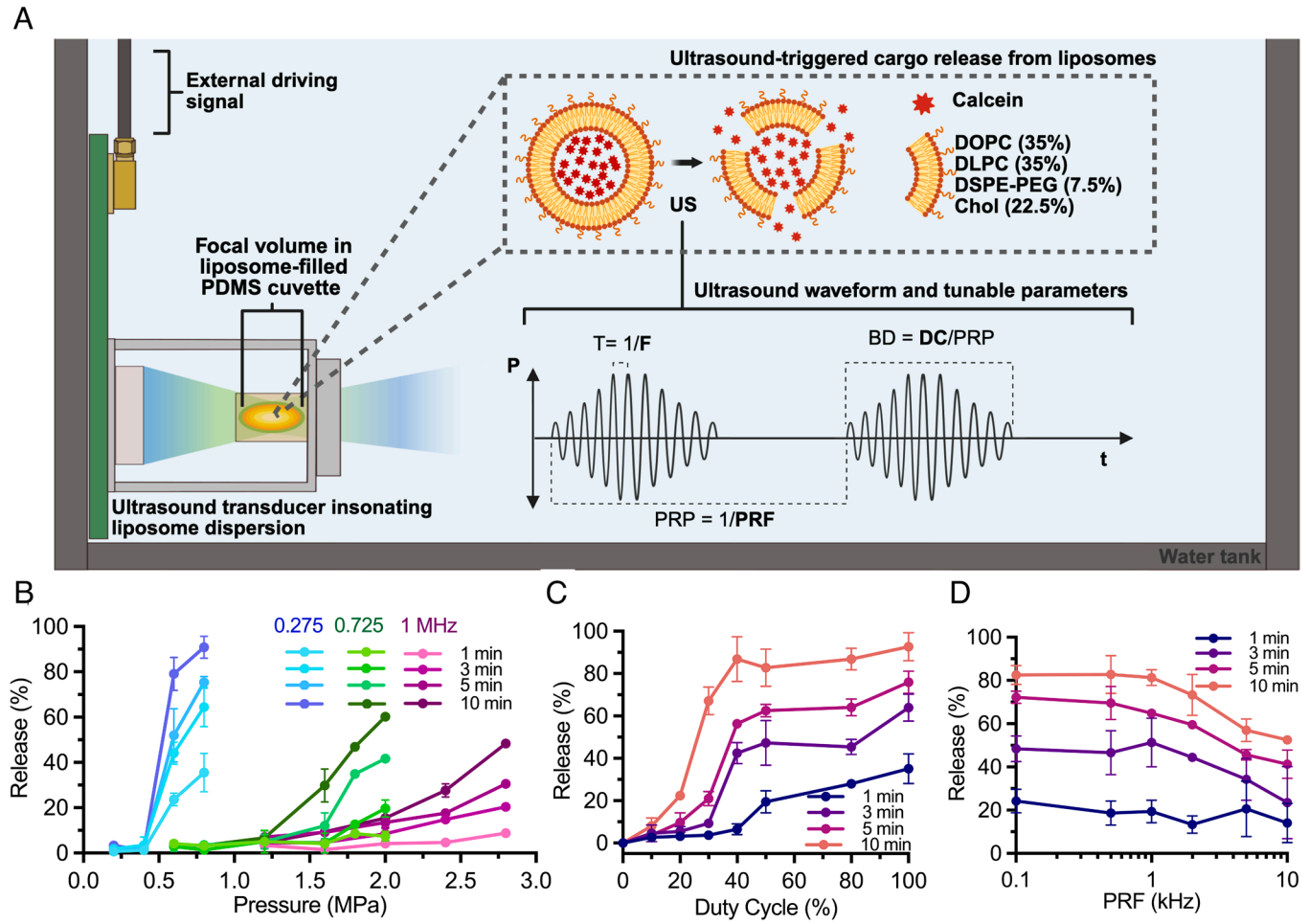


**Fig. 1.** Experimental setup and acoustic parameter dependence of ultrasound-triggered release from liposomes. (*A*) Schematic of the experimental setup used to quantify cargo release. Liposomes containing self-quenched calcein are held in a PDMS cuvette by a custom 3D-printed holder and positioned within the ultrasound focal volume, together submerged in a water tank. The ultrasound beam is generated by a piezoelectric element mounted on a printed circuit board driven by an external signal. Ultrasound parameters such as frequency (F), pressure (P), duty cycle (DC), and pulse repetition frequency (PRF), along with derived quantities such as period (T), pulse repetition period (PRP), and burst duration (BD), are tuned to determine the temporal profile of the ultrasound wave. Detailed descriptions of the ultrasound delivery workflow and transducer configuration are provided in *SI Appendix*, Figs. S2 and S3. (*B*) Release efficiency as a function of $P_{PP}$ at three frequencies (0.275, 0.725, and 1 MHz) for 100% DC, measured after 1, 3, 5, and 10 min of sonication. (*C*) Release efficiency as a function of DC at F = 0.275 MHz, PRF = 1 kHz, and $P_{PP}$ = 0.8 MPa, measured after 1, 3, 5, and 10 min. (*D*) Release efficiency as a function of PRF at F = 0.275 MHz, DC = 50%, and $P_{PP}$=0.8 MPa, measured after 1, 3, 5, and 10 min. Data represent mean ± SD of n ≥3 technical replicates on the same liposome batch. Image partially created with Biorender.com.

To overcome the limitations of previous studies that relied on tip sonicators or commercial transducers with restricted acoustic parameters, a custom ultrasound setup was developed (Fig. 1*A* and *SI Appendix*, Fig. S2). Briefly, lead zirconate titanate-5H (PZT-5H) slabs of varying thicknesses were diced to the desired aperture (*SI Appendix*, Table S1), assembled on printed circuit boards, electrically insulated with Parylene-C, and acoustically characterized through hydrophone measurements. Two-dimensional pressure mapping revealed well-defined ultrasound beams (*SI Appendix*, Fig. S4 *A*–*C*). Thicker PZT elements exhibited lower thickness-mode resonance frequencies of 0.275, 0.725, and 1 MHz for 6-, 2.94-, and 2-mm thicknesses, respectively, as expected from the inverse proportionality between thickness and thickness-mode resonance frequency (*SI Appendix*, Fig. S4*G*). Corresponding −3 dB focal volumes increased with decreasing frequency (*SI Appendix*, Table S1), consistent with greater diffraction and broader acoustic beam propagation at longer wavelengths (46). This underscores the importance of accounting for the focal-volume-to-sample-volume ratio when comparing liposomal release across frequencies, a factor often overlooked in previous studies (39–41). Empirical hydrophone measurements showed a linear relationship between peak-to-peak pressure and voltage from 0 to 80 V, with steeper slopes at higher frequencies (*SI Appendix*, Fig. S4*H*). This behavior is consistent with expectations. Under otherwise identical transducer conditions, shorter wavelengths reduce diffraction, and thinner PZTs tend to convert voltage into acoustic pressure more efficiently (47); consequently, higher acoustic pressures per unit voltage are produced at increasing frequencies.

Custom PDMS cuvettes were fabricated for each frequency, with lateral thickness first calibrated via 3D-printed molds to match the intended geometry (*SI Appendix*, Fig. S5*A*). Cuvette dimensions were then chosen to maintain an 8:1 focal-volume-to-sample-volume ratio across frequencies, thereby balancing minimal beam distortion with the sensitivity required for liposomal release quantification. COMSOL simulations aided the design of 3D-printed holders to ensure reproducible and precise cuvette placement, showing that slight misalignments relative to the focal spot caused considerable beam distortion (*SI Appendix*, Fig. S5 *B*–*D*). Building on this understanding, a custom 3D-printed cuvette holder was engineered to provide accurate alignment in all three axes (X, Y, and Z) with respect to each transducer's beam

profile (*SI Appendix*, Fig. S3). Ultrasound attenuation was then quantified with the cuvette positioned in the holder (*SI Appendix*, Fig. S5 *E*–*G*), revealing pressure reductions of 15.4%, 13.1%, and 12.7% for 0.275, 0.725, and 1 MHz, respectively (*SI Appendix*, Table S1). Accounting for these losses is essential to accurately compare acoustic parameters and establish a mechanistic framework for the influence of acoustic parameters on release efficiency from ultrasound-responsive liposomes. This study comprehensively accounts for beam distortion, focal volume, and sample geometry, enabling meaningful comparison of acoustic parameters and the development of a mechanistic framework for cargo release from ultrasound-responsive liposomes.

**Influence of Pressure and Frequency.** Using the custom ultrasound setup described above, liposomes were insonated at three frequencies (0.275, 0.725, and 1 MHz) over a range of acoustic pressures and durations (1, 3, 5, and 10 min) (Fig. 1*B*). Cargo release was quantified by calcein dequenching, taking advantage of the fluorescence self-quenching effect within liposomal encapsulation. At all frequencies, significant (>5%) release occurred only above a pressure threshold, corresponding to peak-to-peak pressure ($P_{pp}$) values of around 0.42, 1.19, and 1.56 MPa for 0.275, 0.725, and 1 MHz, respectively. This threshold was independent of insonation time. Beyond it, release increased linearly with pressure across all durations. Notably, the slope of this increase was steeper at lower frequencies. This suggests that lower frequencies may not only enable release at lower pressures but also amplify the effect of increasing pressure on the extent of release. These results show a clear frequency and pressure dependence in ultrasound-triggered release (Fig. 1*B*), in agreement with previous work (39), where release increased linearly at 0.3 MHz across all pressure ranges. Other studies also reported greater release efficiency at lower frequencies (39, 41, 48), in alignment with our observations.

To investigate the mechanism of ultrasound-triggered release, particle size was measured before and after insonation, showing no significant change in liposome average size across all ultrasound frequencies, though an increase in PDI was observed at 0.275 MHz (*SI Appendix*, Fig. S6*A*). In addition, release followed first-order kinetics under insonation (*SI Appendix*, Fig. S6*B*) and ceased immediately after ultrasound exposure (*SI Appendix*, Fig. S6*C*). This suggests release occurred via a transient mechanism, such as transient pore formation in the lipid bilayer (i.e., sonoporation), rather than complete vesicle rupture.

**Influence of Duty Cycle and Pulse Repetition Frequency.** The effect of DC was evaluated from 10 to 100% at 0.275 MHz, 0.8 MPa ($P_{pp}$), and a PRF of 1 kHz. This set of ultrasound parameters was selected because it showed an effective induction of ultrasound-triggered release. All insonation times (1 min, 3 min, 5 min, 10 min) yielded a steep increase in release up to 40 to 50% DC, followed by a plateau or slight increase up to 100% DC. This effect was the most pronounced at longer insonation times (Fig. 1*C*). While few studies have systematically examined the influence of DC on release, a linear relationship between 0 and 20% DC has been reported previously, in agreement with our results (39). However, higher DC has not been previously investigated, which we address in this study.

The effect of PRF was evaluated across 0.1 to 10 kHz at 0.275 MHz, 0.8 MPa $P_{pp}$, and 50% DC. The cumulative release remained unchanged between 0.1 to 1 kHz but decreased progressively beyond 1 kHz. The decrease was more pronounced for longer insonation times, with up to ~29% lower release for 10 kHz compared to 1 kHz for 10 min insonation (Fig. 1*D*). The trends differ from those reported previously, where release increased between 50 and 250 Hz before declining up to 350 Hz (33), a discrepancy that could arise from the markedly different ultrasound parameters used (2.8 kW/cm$^2$, 2% DC) and the omission of factors such as acoustic beam distortion or focal volume. Overall, our study demonstrates that increasing the PRF beyond 1 kHz negatively impacts ultrasound-triggered release.

**Acoustic Pressure Oscillations as the Primary Driver for Sonoporation-Facilitated Release.** Ultrasound can exert both thermal and mechanical effects on biological matter (49). Understanding the relative contribution of these effects is essential for developing a mechanistic understanding of different therapeutic ultrasound modalities. For example, clinically translated thermosensitive liposomes, such as ThermoDox® and THE001, rely primarily on local heating to trigger drug release because their membranes contain thermosensitive lipids that undergo a phase transition at hyperthermic temperatures, increasing membrane permeability (9, 10, 50). In contrast, the observed frequency-dependent release (Fig. 1*B*) together with the high cargo retention stability at 37 °C (*SI Appendix*, Fig. S1*F*) and the minimal temperature rise (i.e., up to 2 to 8 °C increase from room temperature with 10 min insonation) measured at the cuvette center using a thermocouple during insonation at 0.275 MHz (*SI Appendix*, Fig. S6*D*) suggests that mechanical effects, rather than thermal effects, are the dominant trigger for the ultrasound-responsive liposomes used in this study. This conclusion is supported by the fact that the thermal index increases with frequency, so if thermal effects were dominant, release would also be expected to rise with frequency. In contrast, the mechanical index (MI) increases with decreasing frequency, which directly corresponds to our observation that lower frequencies produce higher release (Fig. 1*B*).

Elucidating the specific mechanical effects that drive liposome sonoporation is critical to establishing a mechanistic foundation for the effect of acoustic parameters on release. Recent work has demonstrated that direct mechanical interactions of the acoustic field—including acoustic radiation forces and oscillatory acoustic pressure—play a key role in ultrasound-induced biophysical effects (44, 45). To explore ultrasound–liposome interactions, we developed two COMSOL models: one accounting only for oscillatory acoustic pressure by employing a simplified planar wave (Fig. 2*A*) and another accounting also for acoustic radiation force (ARF) by driving a PZT element (Fig. 2*B*).

In both COMSOL models—whether accounting solely for oscillatory particle displacement (Fig. 2*A*) or including both displacement and acoustic radiation force (Fig. 2*B*)—liposome displacement (Fig. 2*C*) and stress (Fig. 2*E*) increased linearly with acoustic pressure, consistent with oscillatory acoustic-pressure-dominated mechanical stress (45). Notably, this trend persisted even for liposomes positioned slightly off the focal spot (*SI Appendix*, Fig. S7), where acoustic radiation forces are stronger, further supporting that oscillatory acoustic pressure is the dominant factor. Both models also exhibited the same frequency-dependent behavior, with displacement amplitudes (Fig. 2*D*) decreasing exponentially and stress remaining constant (Fig. 2*F*) with increasing frequency, again consistent with oscillatory acoustic-pressure-dominated mechanical stress (45). As expected, neither duty cycle (DC) nor pulse repetition frequency (PRF) affected the normalized peak displacement or stress, as these parameters do not modify the instantaneous acoustic waveform but rather its distribution in time (*SI Appendix*, Fig. S8). Overall, the observed behavior across ultrasound parameters is physically reasonable because the liposome diameter is several orders of magnitude smaller than the ultrasound wavelength.

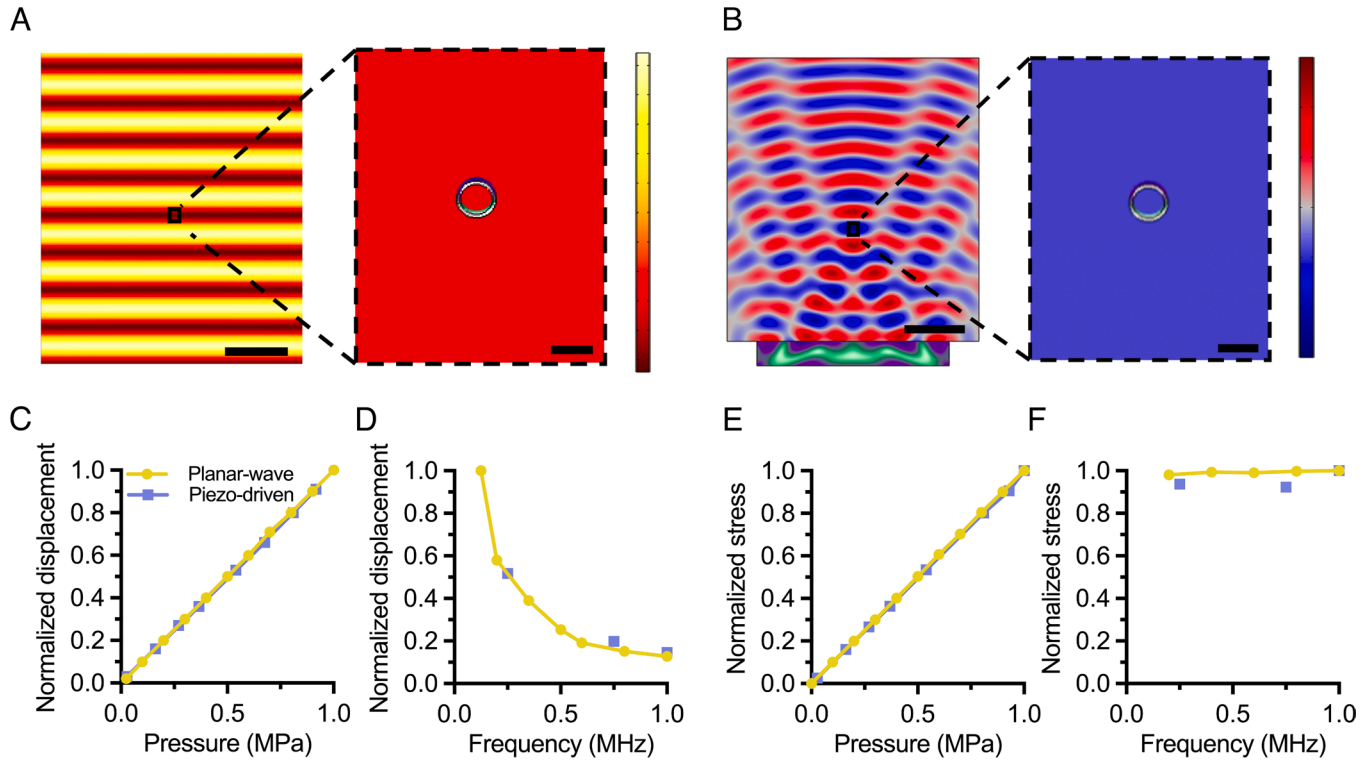


**Fig. 2.** Finite element COMSOL simulations of acoustic field–liposome interactions. (*A* and *B*) Spatial distribution of the acoustic pressure field in the (*A*) sinusoidal planar-wave model representing oscillatory pressure and (*B*) in the piezo-driven ultrasound model with a focused beam geometry, incorporating both oscillatory pressure and radiation. For (*A* and *B*), the color bar goes from normalized $-P_P$ to $P_P$. Scale bars represent 2.8 mm in the overview image and 140 nm in the zoomed-in view. The ring-like structure in the zoomed-in views represents the modeled liposome geometry. (*C* and *D*) Normalized liposome displacement in the planar-wave and piezo-driven model as a function of (*C*) pressure and (*D*) frequency. (*E* and *F*) Normalized stress in the planar-wave and piezo-driven model as a function of (*E*) pressure and (*F*) frequency. Frequency sweeps were performed at $P_{PP}$ = 1 MPa, while pressure sweeps were performed at F = 0.275 MHz. Normalization was performed jointly for both models, using the combined range of model outputs rather than model-specific normalization.

Under these conditions, spatial pressure gradients are negligible. Therefore, liposomes do not effectively feel ARF-related pressure gradients or differences in frequencies, but solely uniform oscillatory pressure-driven stresses. In addition, no complex or asymmetric deformations were observed (*SI Appendix*, Fig. S9), consistent with the liposome being several orders of magnitude smaller than the ultrasound wavelength and therefore experiencing an effectively uniform acoustic field that cannot induce resonance or higher-order vibrational modes. Moreover, we observed no significant difference in release between degassed and nondegassed liposome dispersions (*SI Appendix*, Fig. S6*E*), suggesting that cavitation, which is more difficult to initiate in liquids with lower dissolved gas content due to the scarcity of preexisting nuclei (51), is unlikely to be the dominant mechanism under our experimental conditions. It should be noted that our approach does not rule out the possibility of cavitation, and we acknowledge that some residual cavitation could potentially contribute to cargo release. Nevertheless, previous studies on ultrasound-triggered release from liposomes have already demonstrated that cavitation typically plays a minor role in these systems (23, 52). Overall, our results suggest that pressure-induced oscillatory mechanical forces appear to dominate over acoustic radiation forces.

Having identified mechanical effects as the main driver of release, we investigated the response of the lipid bilayer under mechanical perturbation. Pressure-dependent bilayer response was investigated with coarse-grained molecular dynamics simulations on a model lipid bilayer matching the experimental ultrasound-responsive formulation (Fig. 3). Pore formation under increasing pressures was quantified by the change in relative water density inside the bilayer compared to the surrounding bulk as a function of time (53) (Fig. 3*A*). Pores appeared only above a threshold pressure (Fig. 3 *B*–*F*). In addition, higher pressures induced a faster and greater number of pores (Fig. 3 *G*–*K*), inducing earlier and more extensive pore formation, with pores continuing to enlarge under sustained pressure. This is in line with our empirical observations (Fig. 1*B*). That said, it should be noted that onset pressures in the molecular dynamics simulations were higher than those applied experimentally, likely due to differences in how mechanical stress was imposed in simulations compared to real ultrasound environments. Consequently, our simulation pressures are intended to provide a qualitative assessment of pressure-induced liposomal bilayer response, rather than a quantitative reproduction of experimental pressure values. The observed results are in line with previous atomistic and coarse-grained simulation (54–56) studies showing that hydrophilic pore formation occurs under membrane tension (57, 58), with relative water density inside the bilayer rising as a function of pressure (53). Overall, molecular dynamics simulations support transient pore formation as the dominant pressure-dependent mechanism in ultrasound-triggered release of PEGylated liposomes.

## Discussion

**Mechanistic Framework Linking Acoustic Parameters to Release in Ultrasound-Responsive Liposomes.** The experimental and computational results suggest that sonoporation-facilitated release occurs only above a critical pressure threshold ($P_{THR}$). This is consistent with pore formation theory in lipid membranes, where sufficient energy is required to overcome the energy barrier of pore formation (59, 60). Ultrasound waves can be simplified as a sinusoidal pressure wave alternating in a frequency-dependent

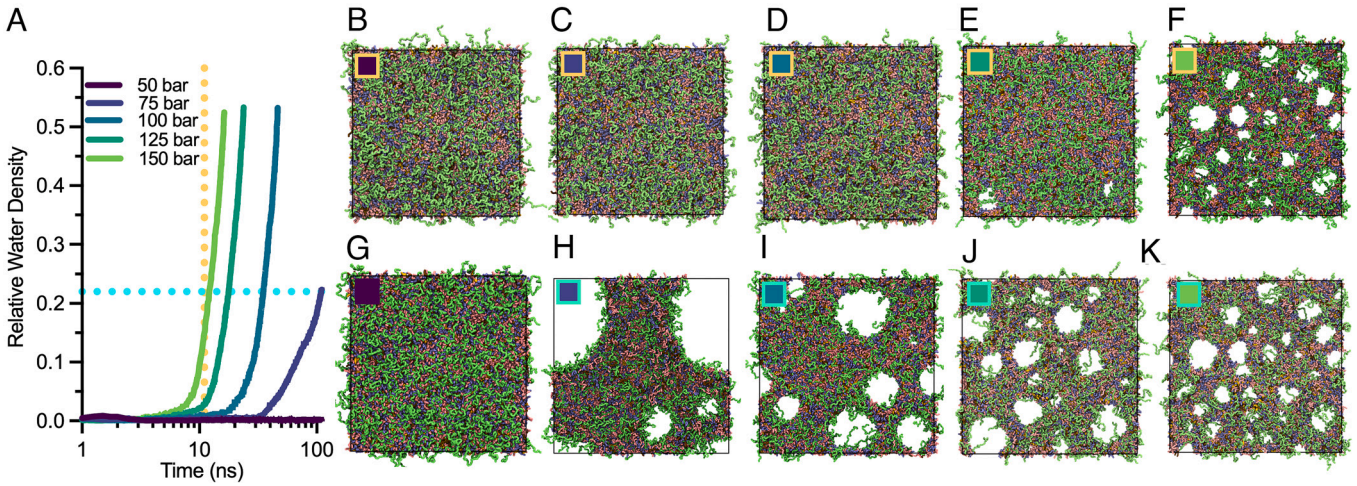


**Fig. 3.** Coarse-grain molecular dynamics simulations of a model lipid bilayer under pressure perturbation. (*A*) Relative water density in bilayer pores as a function of simulation time under increasing pressures (50 to 150 bar), obtained from coarse-grained molecular dynamics simulations. The vertical dashed yellow line indicates a reference time of 11 ns, and the horizontal cyan line marks a reference relative water density of 0.225; these lines serve as visual references for the snapshots shown in panels *B*–*K*. (*B*–*F*) Bilayer configurations at 11 ns for pressures of (*B*) 50 bar, (*C*) 75 bar, (*D*) 100 bar, (*E*) 125 bar, and (*F*) 150 bar. (*G*–*K*) Representative configurations shown for comparison at a relative water density of 0.225 for (*H*) 75 bar, (*I*) 100 bar, (*J*) 125 bar, and (*K*) 150 bar; for 50 bar (*G*), no pore formation was observed, and the snapshot corresponds to the final simulation frame (100 ns) instead. In panels *B*–*K*, squares mark the corresponding data points in panel *A*; the inner color shows which pressure curve the snapshot represents, and the outer color indicates the reference line (yellow: 11 ns; cyan: relative water density 0.225). Box dimensions vary among snapshots (*SI Appendix*, Table S2) but are shown at a fixed scale and without water beads for clarity.

manner between $P_{peak}$ and $-P_{peak}$, with a build-up and decay phase (Fig. 4*A*). Higher pressures straightforwardly increase the time $|P| > P_{THR}$. Frequency plays a less intuitive but critical role. In the proposed framework, sonoporation depends not only on the total time spent above $P_{THR}$ but also on the duration of each continuous suprathreshold interval, since longer uninterrupted exposure increases the likelihood of pore nucleation and subsequent expansion events. Lower frequencies prolong each oscillation above $P_{THR}$, increasing the likelihood of pore nucleation and expansion during a single cycle, whereas higher frequencies produce more cycles per unit time, but each spends less time above $P_{THR}$, thus lowering the likelihood of pore formation and expansion. Consequently, lower frequencies and higher pressures concomitantly produce more efficient pore formation and expansion, consistent with the experimentally observed increase in release at lower frequencies and increased pressures (Fig. 1*B*).

The temporal build-up and decay phases become relevant when considering the PRF and DC. During these transient phases, $|P| < P_{THR}$, and pore formation cannot occur (Fig. 4*A*). Varying the PRF does not change the total number of oscillation cycles delivered, but it redistributes them in time. At higher PRFs, pulses occur more frequently and with shorter spacing, increasing the relative fraction of each pulse occupied by build-up and decay phases, which reduces the effective time during which $|P| > P_{THR}$ (Fig. 4*B*). Consequently, pore formation and release efficiency decrease with increasing PRF due to the increased relative contribution of build-up and decay phases. Minor PRF changes (e.g., 0.1 to 0.2 kHz) have negligible effects on the effective duration in which $|P| > P_{THR}$, whereas larger increases (e.g., 1 to 5 kHz) markedly shorten it, aligning with the experimentally observed decline in release (Fig. 1*D*). On the other hand, increasing the DC extends the cumulative duration during which $|P| > P_{THR}$, promoting successive nucleation and expansion of transient pores (Fig. 4*B*). This leads to the observed near-linear enhancement in release up to ~50% DC (Fig. 1*C*). Beyond this point, it is proposed that the liposomes approach a saturation point where most pores have already formed and stabilized near their maximal thermodynamically stable size. Further increases in DC thus yield small increases in release, as the membrane reaches a quasi-steady state of pore activity per burst, consistent with the experimental observations.

In addition, we hypothesize that this framework could also be employed to explain the effect of lipid composition on ultrasound-responsivity by modulating $P_{THR}$ in a formulation-dependent manner, thereby altering pore formation dynamics due to the time fraction in which $|P| > P_{THR}$. For instance, modifying the lipid headgroup type (28), incorporating targeting moieties (29), or adding lysolipids (61) might have increased ultrasound-responsivity by lowering $P_{THR}$, thereby increasing the duration for which $|P| > P_{THR}$. This aligns with recent findings showing that lipid composition governs pore formation in complex biological membranes (62). In that sense, $P_{THR}$ serves an analogous role to the free energy of pore formation in classical pore formation theory but offers a more practical descriptor for ultrasound-responsive liposomes under acoustic insonation. Thus, this framework could potentially unify acoustic parameter selection with liposome formulation optimization for enhanced ultrasound-triggered release efficiency. Exploring this from a mechanistic point of view for PEGylated lipids, which have been demonstrated to be essential for improved ultrasound-responsivity (25), will be the focus of future studies.

**Implications for Clinical Translation.** According to the experimental results and mechanistic framework, lower frequencies, higher pressures, low PRFs, and DC above 40% yield maximal release from ultrasound-responsive liposomes. However, the experiments in this study were conducted under simplified conditions that are not representative of in vivo settings. After intravenous administration, liposomes circulate through the bloodstream and release the cargo when passing through the sonoporation active volume (SAV). The SAV is defined here as the three-dimensional spatial region where the acoustic pressure magnitude $|P|$ exceeds the critical threshold $P_{THR}$, sufficient to induce ultrasound-driven transient pore formation in the liposome bilayer and the consequent drug release. Visually, the SAV is similar to the focal volume, but its boundaries are determined specifically by $P_{THR}$. While unlikely

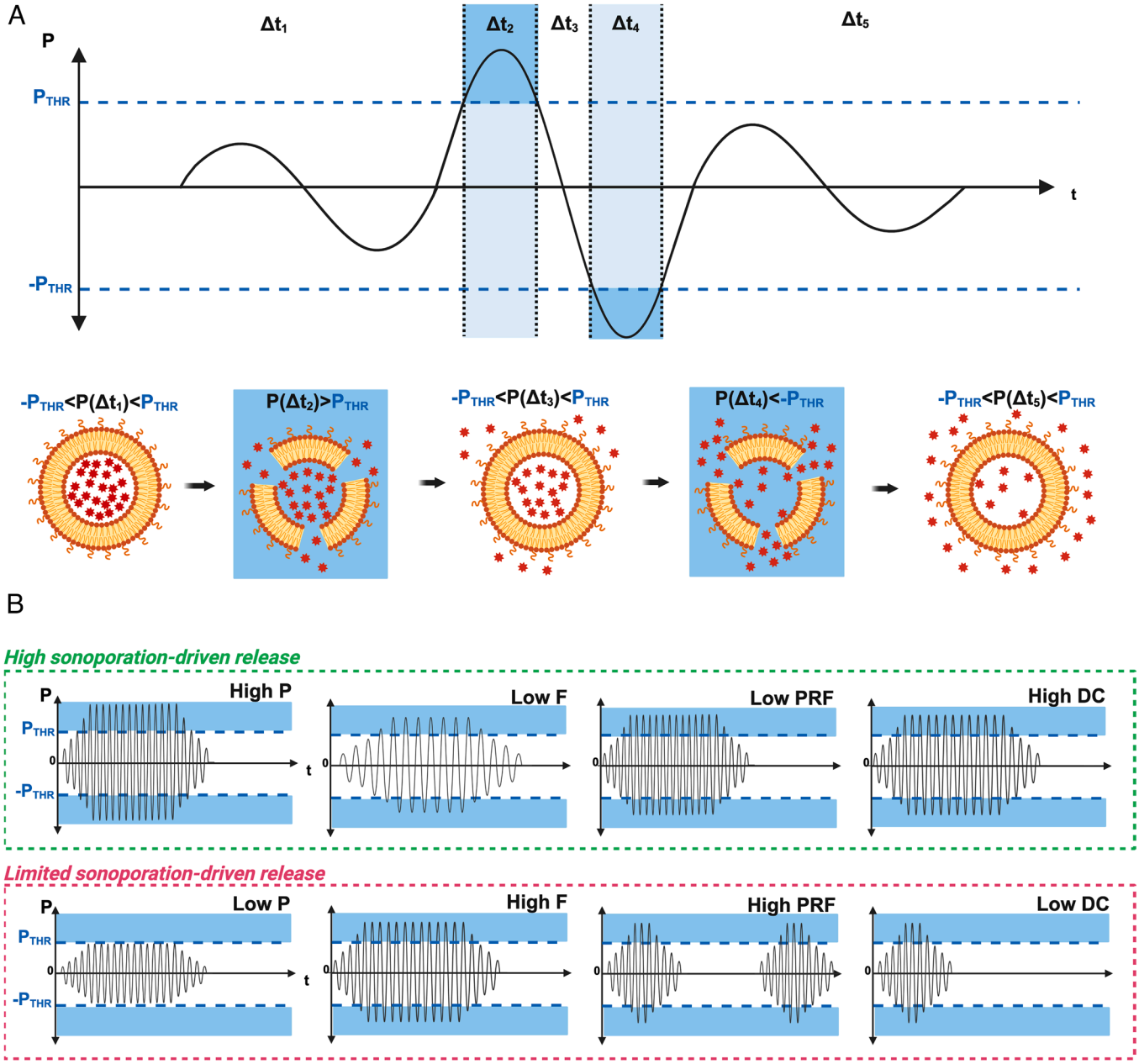


**Fig. 4.** Mechanistic framework on the modulation of release dynamics by acoustic parameters in ultrasound-induced sonoporation in ultrasound-responsive PEGylated liposomes. (*A*) Schematic representation of a sinusoidal acoustic pressure wave with build-up and decay phases and its relationship with the critical pressure threshold for pore formation ($P_{THR}$). Shaded regions indicate the time portion for which $|P| > P_{THR}$ (i.e., $P > P_{THR}$ or $P < -P_{THR}$), enabling pore nucleation and expansion. The accompanying cartoons depict the state of the liposomal membrane during each corresponding pressure region, illustrating how pore-driven release varies over time as a function of the relationship between P and $P_{THR}$. (*B*) Schematics showing how P, F, PRF, and DC shape the time intervals during which the acoustic waveform exceeds $\pm P_{THR}$, thereby influencing the likelihood of pore formation and expansion and resulting release. Higher P increases release by enlarging the portion of each oscillation during which $|P| > P_{THR}$. Lower F increases release by lengthening each oscillation, which increases the time per cycle spent above $P_{THR}$ and thereby raises the likelihood of both pore nucleation and subsequent pore expansion. Lower PRF increases release by reducing the relative contribution of the build-up and decay phases within each pulse, thereby increasing the fraction of the burst during which $|P| > P_{THR}$. Higher DC increases release by prolonging the overall cumulative exposure time during which $|P| > P_{THR}$. Image created with Biorender.com.

to alter the pressure- and frequency-dependent trends, it could diminish the relevance of PRF while making higher DC more important to ensure sufficient pore-opening times as liposomes traverse the SAV. Nevertheless, increasing the DC in vivo must be done cautiously, as it raises the risk of mechanical and thermal tissue damage. For example, at 0.275 MHz, 50% DC, PRF 1 kHz, and $P_{PP}$ 0.8 MPa—conditions under which we observed some of the highest cargo release (Fig. 1)—we measured a local temperature increase of approximately 4 °C after 10 min of insonation (*SI Appendix*, Fig. S6*D*). Under these parameters, the spatial peak temporal average intensity ($I_{SPTA}$) and MI were 2.48 W/cm$^2$ and 0.76, respectively. The MI was well below the FDA-established safety threshold for diagnostic ultrasound (MI < 1.9), and the $I_{SPTA}$ was substantially lower than commonly employed in clinical thermal ablation and at the lower end of the range reported to induce reversible neuromodulation (63, 64).

While the utilized pressures in this study are approximately 2 orders of magnitude lower than those typically employed in clinical high-intensity focused ultrasound applications (65), which can reach tens of MPa at the focal spot, potential local heating,

skin irritation, or discomfort would need to be carefully evaluated to improve patient outcomes (66). Additionally, energy dissipation within tissue—through absorption and scattering—can reduce the effective acoustic pressure at depth, particularly for deep targets, and may also contribute to heating along the propagation path, with higher pressures and frequencies increasing the energy deposited. Thus, an optimal balance between acoustic pressure and DC, at low frequencies, must be achieved to maximize release efficiency without compromising safety. For example, one may envision utilizing a clinical system like InSightec's ExAblate platform, extended beyond neuro applications (67). Such a transducer can operate at low- and high-intensity modes at 220 kHz and 650 kHz, respectively. Based on our results, because release increases with both lower frequency and higher pressures, low-frequency low-intensity operation may achieve comparable cumulative release to high-frequency high-intensity operation. The lower frequency would also likely allow higher DC within clinical safety limits, further increasing cumulative release. Thus, from a parameter-selection standpoint, the lower-frequency operation, which enables lower intensity conditions, may represent a more promising regime for ultrasound-triggered drug release from liposomes, provided that mechanical effects and associated tissue damage are carefully considered.

Transducer design must also align with the optimal acoustic conditions. Although low frequencies favor release, practical constraints arise because piezoelectric ultrasound transducers require proportionally larger apertures to maintain maximum focal depth at lower frequencies. In other words, frequencies cannot be decreased arbitrarily, as excessively low frequencies result in negligible focal depth and the loss of a defined focal volume, making deep-tissue targeting unfeasible. This is the case for tip sonicators operating at 20 to 50 kHz. For example, for the 0.275 MHz planar transducer that yielded the highest release in this study, achieving a 25 cm focal depth would require an aperture of approximately 7.5 cm based on the near-field approximation. This provides a lower-bound estimate, implying that transducers, when focused, require even larger apertures to achieve the same deep focal depth with increased pressure. Such apertures are practical for a stereotactic configuration in clinics, but they limit the use of wearable or implantable devices. Furthermore, the geometry of the SAV could be another critical design factor. Larger SAVs could enhance release within the target area by increasing the probability of liposomes experiencing threshold-exceeding pressures, but overly broad volumes risk off-target effects. Shaping of the focal volume through phased arrays, phase- and amplitude-modulated acoustic holograms, or multitransducer stereotactic configurations, as opposed to hand-held probes, could enable the required precise control over the spatial and temporal distribution of the SAV. Ultimately, successful clinical translation of ultrasound-responsive liposomes will require ultrasound transducers operating at parameters that maximize release, alongside careful optimization of focal volume, spatial precision, and tissue safety to enhance therapeutic index while minimizing adverse effects.

In conclusion, based on computational modeling and experimental validation, we propose a sonoporation-based framework to explain how acoustic parameters influence ultrasound-triggered release from liposomes. Specifically, we hypothesize that release efficiency is determined by the duration that the ultrasound wave remains above a critical $P_{THR}$ necessary to induce poration in the liposomal bilayer, which can be tuned through different acoustic settings. These mechanistic insights can inform the rational design of ultrasound transducers and support the clinical translation of PEGylated ultrasound-responsive liposomes.

## Materials and Methods

**Liposome Synthesis and Characterization.** Further details are provided in the *SI Appendix*. Liposomes were prepared using the thin-film hydration method (68). Briefly, DLPC:DOPC:Cholesterol:DSPE-PEG2000 35:35:22.5:7.5 mol% (Avanti Polar Lipids) were dissolved in chloroform. The solvent was evaporated using a rotary evaporator (Rotavapor R-100 with V-100 pump, Büchi) and under high vacuum (CRVpro 4, Welch). The resulting dry lipid film was hydrated with a 50 mM calcein solution prepared in phosphate-buffered saline (PBS, 10 mM, pH 7.4), and its size was reduced by extrusion using a Mini-Extruder (Avanti Polar Lipids). Nonencapsulated calcein was removed by dialysis (MWCO 1,000 kDa membranes, Spectra/Por Biotech).

Total lipid content was quantified using the Stewart assay (69). Dye encapsulation efficiency was determined by disrupting liposomes in a 1:1 (v/v) THF-PBS mixture and measuring calcein absorbance (NanoDrop 2000c, Thermo Fisher). Size and ζ-potential were measured on a Zetasizer Nano ZS (Malvern Panalytical). Cryogenic transmission electron microscopy (cryo-TEM) was performed at 120 kV (626 cryoholder, Gatan; F416 camera, TVIPS).

**Ultrasound Transducer Fabrication and Characterization.** Further details are provided in the *SI Appendix*. Custom single-element ultrasound transducers were fabricated using PZT-5H ceramic plates (Piezo.com; Zibo Yuhai Electronic Ceramic Co., Ltd). Each slab was diced to the target aperture using a precision dicing saw (DAD3240, Disco) (*SI Appendix*, Table S1). The PZT element was mechanically bonded to a custom printed circuit board (PCB) with conductive epoxy (EPO-TEK H20E, Epoxy Technology), establishing the bottom plate electrical driving connection. Ground electrical connections were completed by bonding 0.05 mm-diameter tungsten wires between the PZT top surface and the PCB ground contact pad. The assembled transducer was coated with Parylene-C (PDS 2010 Labcoter 3, SCS) for electrical insulation. PDMS cuvettes and matching holders were designed in Fusion 360, 3D-printed in polylactic acid (PLA) (Bambu Lab X1 Carbon), and cast with a 7:1 PDMS:curing-agent mixture. After degassing and curing, cuvettes were cleaned with sequential THF-acetone baths and sealed. Cuvette wall thickness and size were optimized via calibration curves from printed test molds (*SI Appendix*, Fig. S5*A*).

Acoustic field mapping was performed in deionized water using a fiber-optic hydrophone (FOHS V2, Precision Acoustics) on a 3-axis motorized stage (VK-62000, GAMPT). Hydrophone signals were recorded with a digital oscilloscope (DSO-X 3032A, Keysight) and controlled through a custom MATLAB interface (R2022b, MathWorks). Pressure maps were collected to determine resonance frequency, focal distance, and −3 dB focal volume by mapping 2D planes parallel to the transducer and lines perpendicular to it. PDMS cuvette placement was optimized to fully encapsulate the focal volume with minimal beam distortion. Linearity of voltage-to-pressure response was verified up to 80 V using a power amplifier (AG Series, T&C Power Conversion).

**Ultrasound-Triggered Release Experiments.** Further details are provided in the *SI Appendix*. PDMS cuvettes were filled with liposome dispersion and the assembled cuvette-holder-transducer unit was submerged in a 3D-printed PLA water tank. Ultrasound pulses were generated via a function generator (DG4202, RIGOL) and amplified (AG Series, T&C Power Conversion), with waveform parameters controlled through a custom MATLAB interface. After insonation, samples were analyzed by fluorescence spectrophotometry (J-815 CD, JASCO). Cumulative release was calculated by calcein dequenching as $R(\%) = (F-F_n)/(F_p-F_n) \times 100$, where $F$, $F_n$, and $F_p$ correspond to fluorescence after insonation, negative control (uninsonated), and positive lyzed control, respectively. Sample temperature during insonation was measured with a thermocouple (179 True-RMS Multimeter, Fluke).

**COMSOL and Molecular Dynamics Simulations.** Further details are provided in the *SI Appendix*. Two finite-element models were developed in COMSOL Multiphysics 6.2. The first employed a simplified planar wave to isolate the effect of oscillatory acoustic pressure, while the second included acoustic radiation force by explicitly modeling a PZT-5H transducer driven by a sinusoidal voltage. Both used the Transient Pressure Acoustics and Solid Mechanics modules coupled through acoustic-structure boundaries. The liposome was modeled as a viscoelastic spherical shell immersed in water. Perfectly matched layers were used to prevent reflections at domain boundaries. Simulations were performed

in the time domain with an adaptive mesh to consider wavelength and lipid bilayer thickness.

Further details are provided in the *SI Appendix*. Molecular dynamics simulations were performed in GROMACS 2025.1 (70, 71) using the Martini 3 coarse-grained force field (72). Symmetric bilayers composed of DLPC:DOPC:Cholesterol:DSPE-PEG2000 35:35:22.5:7.5 mol% were generated using INSANE (73) and Polyply (74). The simulation box contained 70,381 water beads (~13:1 water-to-lipid ratio). The negatively charged DSPE-PEG2000 lipopolymers were neutralized by 404 Na ions for charge neutrality. Following energy minimization, equilibration proceeded through sequential NVT and NPT stages with increasing time steps and a final 10 ns of equilibration with semi-isotropic pressure coupling. Production runs applied a lateral pressure of 1 bar, while the pressure normal to the bilayer was kept constant in each simulation and set to values between 50 and 150 bar. Snapshots were generated using MartiniGlass (75) and Visual Molecular Dynamics (76).

**Data, Materials, and Software Availability.** All study data are included in the article and/or *SI Appendix*.

**ACKNOWLEDGMENTS.** This work was supported by the Convergence Health and Technology, the alliance between Erasmus Medical Centre Rotterdam, Erasmus University Rotterdam, and Delft University of Technology. This work was supported by the project UPSIDE (ID 101070931), which has received funding within the framework of Horizon EIC 2021 Pathfinder Challenges by the European Union. We gratefully acknowledge Dr. Telesilla Bristogianni for her assistance with sample dicing, Dr. Wiel Evers for support with Cryo-EM imaging, and Dr. Pouyan Boukani for his fruitful discussions on lipid bilayer poration. We acknowledge the use of computational resources of the DelftBlue supercomputer, provided by Delft High Performance Computing Centre (https://www.tudelft.nl/dhpc).

Author affiliations: [a]Department of Chemical Engineering, Delft University of Technology, Delft 2629 HZ, the Netherlands; [b]Department of Microelectronics, Delft University of Technology, Delft 2628 CD, the Netherlands; [c]Department of Process and Energy, Delft University of Technology, Delft 2628 CB, the Netherlands; and [d]Department of Chemical Engineering, KU Leuven, Leuven 3001, Belgium

1. L. M. Liz-Marzán *et al.*, What do we mean when we say nanomedicine? *ACS Nano* **16**, 13257–13259 (2022).
2. M. T. Manzari *et al.*, Targeted drug delivery strategies for precision medicines. *Nat. Rev. Mater.* **6**, 351–370 (2021).
3. M. J. Mitchell *et al.*, Engineering precision nanoparticles for drug delivery. *Nat. Rev. Drug Discov.* **20**, 101–124 (2021).
4. S. Roovers *et al.*, The role of ultrasound-driven microbubble dynamics in drug delivery: From microbubble fundamentals to clinical translation. *Langmuir* **35**, 10173–10191 (2019).
5. H. Nsairat *et al.*, Liposomes: Structure, composition, types, and clinical applications. *Heliyon* **8**, e09394 (2022).
6. V. P. Torchilin, Recent advances with liposomes as pharmaceutical carriers. *Nat. Rev. Drug Discov.* **4**, 145–160 (2005).
7. Y. Barenholz, Doxil®–The first FDA-approved nano-drug: Lessons learned. *J. Control. Release* **160**, 117–134 (2012).
8. Y. Lee, D. H. Thompson, Stimuli-responsive liposomes for drug delivery. *WIREs Nanomed. Nanobiotechnol.* **9**, e1450 (2017).
9. R. M. Pallares, R. A. Barmin, A. Wang, F. Kiessling, T. Lammers, Clinical cancer nanomedicines. *J. Control. Release* **385**, 113991 (2025).
10. Y. Dou, K. Hynynen, C. Allen, To heat or not to heat: Challenges with clinical translation of thermosensitive liposomes. *J. Control. Release* **249**, 63–73 (2017).
11. N. S. Awad *et al.*, Ultrasound-responsive nanocarriers in cancer treatment: A review. *ACS Pharmacol. Transl. Sci.* **4**, 589–612 (2021).
12. W. D. O'Brien, Ultrasound–biophysics mechanisms. *Prog. Biophys. Mol. Biol.* **93**, 212–255 (2007).
13. J. Blackmore, S. Shrivastava, J. Sallet, C. R. Butler, R. O. Cleveland, Ultrasound neuromodulation: A review of results, mechanisms and safety. *Ultrasound Med. Biol.* **45**, 1509–1536 (2019).
14. Z. Xu, T. D. Khokhlova, C. S. Cho, V. A. Khokhlova, Histotripsy: A method for mechanical tissue ablation with ultrasound. *Annu. Rev. Biomed. Eng.* **26**, 141–167 (2024).
15. Y.-F. Zhou, High intensity focused ultrasound in clinical tumor ablation. *World J. Clin. Oncol.* **2**, 8–27 (2011).
16. E. E. Konofagou *et al.*, Ultrasound-induced blood-brain barrier opening. *Curr. Pharm. Biotechnol.* **13**, 1332–1345 (2012).
17. K. B. Bader, G. Bouchoux, C. K. Holland, "Sonothrombolysis" in *Therapeutic Ultrasound*, A. Bouakaz, J.-M. Escoffre, Ed. (Springer International Publishing, 2016), pp. 339–362.
18. L. di Biase *et al.*, Focused ultrasound (FUS) for chronic pain management: Approved and potential applications. *Neurol. Res. Int.* **2021**, 8438498 (2021).
19. S. Mitragotri, Healing sound: The use of ultrasound in drug delivery and other therapeutic applications. *Nat. Rev. Drug Discov.* **4**, 255–260 (2005).
20. P. Zhu, I. Simon, I. Kokalari, D. S. Kohane, A. Y. Rwei, Miniaturized therapeutic systems for ultrasound-modulated drug delivery to the central and peripheral nervous system. *Adv. Drug Deliv. Rev.* **208**, 115275 (2024).
21. A. Schroeder, J. Kost, Y. Barenholz, Ultrasound, liposomes, and drug delivery: Principles for using ultrasound to control the release of drugs from liposomes. *Chem. Phys. Lipids* **162**, 1–16 (2009).
22. W. N. Bahutair, W. H. Abuwatfa, G. A. Husseini, Ultrasound triggering of liposomal nanodrugs for cancer therapy: A review. *Nanomaterials* **12**, 3051 (2022).
23. M. P. Purohit *et al.*, Acoustically activatable liposomes as a translational nanotechnology for site-targeted drug delivery and noninvasive neuromodulation. *Nat. Nanotechnol.* **20**, 1688–1699 (2025).
24. R. A. Barmin *et al.*, Polymeric materials for ultrasound imaging and therapy. *Chem. Sci.* **14**, 11941–11954 (2023).
25. A. Schroeder *et al.*, Controlling liposomal drug release with low frequency ultrasound: Mechanism and feasibility. *Langmuir* **23**, 4019–4025 (2007).
26. G. Enden, A. Schroeder, A mathematical model of drug release from liposomes by low frequency ultrasound. *Ann. Biomed. Eng.* **37**, 2640–2645 (2009).
27. H.-Y. Lin, J. L. Thomas, Factors affecting responsivity of unilamellar liposomes to 20 kHz ultrasound. *Langmuir* **20**, 6100–6106 (2004).
28. N. S. Awad, V. Paul, N. M. AlSawaftah, G. A. Husseini, Effect of phospholipid head group on ultrasound-triggered drug release and cellular uptake of immunoliposomes. *Sci. Rep.* **13**, 16644 (2023).
29. N. S. Awad *et al.*, Effect of pegylation and targeting moieties on the ultrasound-mediated drug release from liposomes. *ACS Biomater. Sci. Eng.* **6**, 48–57 (2020).
30. N. M. AlSawaftah *et al.*, Ultrasound-sensitive cRGD-modified liposomes as a novel drug delivery system. *Artif. Cells Nanomed. Biotechnol.* **50**, 111–120 (2022).
31. A. Schroeder *et al.*, Ultrasound triggered release of cisplatin from liposomes in murine tumors. *J. Control. Release.* **137**, 63–68 (2009).
32. A. Elamir *et al.*, Ultrasound-triggered herceptin liposomes for breast cancer therapy. *Sci. Rep.* **11**, 7545 (2021).
33. Y.-S. Kim *et al.*, Ultrasound-responsive liposomes for targeted drug delivery combined with focused ultrasound. *Pharmaceutics* **14**, 1314 (2022).
34. C. Hu *et al.*, Low-intensity focused ultrasound-responsive phase-transitional liposomes loaded with STING agonist enhances immune activation for breast cancer immunotherapy. *Cancers* **16**, 3657 (2024).
35. T. J. Evjen *et al.*, In vivo monitoring of liposomal release in tumours following ultrasound stimulation. *Eur. J. Pharm. Biopharm.* **84**, 526–531 (2013).
36. S. Eggen *et al.*, "Ultrasound mediated delivery of liposomal doxorubicin in prostate tumor tissue" in *2012 IEEE International Ultrasonics Symposium* (2012), pp. 436–439.
37. J. He *et al.*, Tuning the fluidity and protein corona of ultrasound-responsive liposomal nanovaccines to program T cell immunity in mice. *Nat. Commun.* **15**, 8121 (2024).
38. A. Y. Rwei *et al.*, Ultrasound-triggered local anaesthesia. Nat. *Biomed. Eng.* **1**, 644–653 (2017).
39. M. Afadzi *et al.*, Effect of ultrasound parameters on the release of liposomal calcein. *Ultrasound Med. Biol.* **38**, 476–486 (2012).
40. F. El Hajj *et al.*, Molecular study of ultrasound-triggered release of fluorescein from liposomes. *Langmuir* **37**, 3868–3881 (2021).
41. M. Pong *et al.*, In vitro ultrasound-mediated leakage from phospholipid vesicles. *Ultrasonics* **45**, 133–145 (2006).
42. W. Legon, A. Strohman, Low-intensity focused ultrasound for human neuromodulation. *Nat. Rev. Methods Primers* **4**, 91 (2024).
43. S. Yoo, D. R. Mittelstein, R. C. Hurt, J. Lacroix, M. G. Shapiro, Focused ultrasound excites cortical neurons via mechanosensitive calcium accumulation and ion channel amplification. *Nat. Commun.* **13**, 493 (2022).
44. T. Nandi, B. R. Kop, K. Butts Pauly, C. J. Stagg, L. Verhagen, The relationship between parameters and effects in transcranial ultrasonic stimulation. *Brain Stimul.* **17**, 1216–1228 (2024).
45. T. Nandi *et al.*, Biophysical effects and neuromodulatory dose of transcranial ultrasonic stimulation. *Brain Stimul.* **18**, 659–664 (2025).
46. T. Costa *et al.*, An integrated 2D ultrasound phased array transmitter in CMOS with pixel pitch-matched beamforming. *IEEE Trans. Biomed. Circuits Syst.* **15**, 731–742 (2021).
47. H. Sadeghi Gougheri, A. Dangi, S.-R. Kothapalli, M. Kiani, A comprehensive study of ultrasound transducer characteristics in microscopic ultrasound neuromodulation. *IEEE Trans. Biomed. Circuits Syst.* **13**, 835–847 (2019).
48. N. M. AlSawaftah, V. Paul, N. S. Awad, G. A. Husseini, Effect of high-frequency ultrasound on targeted liposomes. *J. Biomed. Nanotechnol.* **18**, 1793–1804 (2022).
49. Z. Izadifar, P. Babyn, D. Chapman, Mechanical and biological effects of ultrasound: A review of present knowledge. *Ultrasound Med. Biol.* **43**, 1085–1104 (2017).
50. M. Regenold *et al.*, Turning down the heat: The case for mild hyperthermia and thermosensitive liposomes. *Nanomedicine (Lond.).* **40**, 102484 (2022).
51. T. Leighton, "The acoustic bubble" in *Journal of The Acoustical Society of America* (1994).
52. C. Oerlemans, R. Deckers, G. Storm, W. E. Hennink, J. F. W. Nijsen, Evidence for a new mechanism behind HIFU-triggered release from liposomes. *J. Control. Release.* **168**, 327–333 (2013).
53. H. Leontiadou, A. E. Mark, S. J. Marrink, Molecular dynamics simulations of hydrophilic pores in lipid bilayers. *Biophys. J.* **86**, 2156–2164 (2004).
54. A. T. N. Vo, M. A. Murphy, P. K. Phan, R. K. Prabhu, T. W. Stone, Effect of force field resolution on membrane mechanical response and mechanoporation damage under deformation simulations. *Mol. Biotechnol.* **66**, 865–875 (2024).
55. W. F. D. Bennett, D. P. Tieleman, Water defect and pore formation in atomistic and coarse-grained lipid membranes: Pushing the limits of coarse graining. *J. Chem. Theory Comput.* **7**, 2981–2988 (2011).
56. S. A. Kirsch, R. A. Böckmann, Membrane pore formation in atomistic and coarse-grained simulations. *Biochim. Biophys. Acta, Biomembranes* **1858**, 2266–2277 (2016).
57. H. Lee, H. Moon, H.-R. Kim, Effects of lipid shape and interactions on the conformation, dynamics, and curvature of ultrasound-responsive liposomes. *Pharmaceutics* **14**, 1512 (2022).
58. V. H. Man, M. S. Li, J. Wang, P. Derreumaux, P. H. Nguyen, Interaction mechanism between the focused ultrasound and lipid membrane at the molecular level. *J. Chem. Phys.* **150**, 215101 (2019).
59. S. A. Akimov *et al.*, Pore formation in lipid membrane II: Energy landscape under external stress. *Sci. Rep.* **7**, 12509 (2017).

60. S. A. Akimov *et al.*, Pore formation in lipid membrane I: Continuous reversible trajectory from intact bilayer through hydrophobic defect to transversal pore. *Sci. Rep.* **7**, 12152 (2017).
61. S. Kim *et al.*, Tumor suppression effect of ultrasound-sensitive nanoparticles with focused ultrasound in a pancreas cancer xenograft model. *Eur. Radiol. Exp.* **8**, 39 (2024).
62. L. J. Starke, C. Allolio, J. S. Hub, How pore formation in complex biological membranes is governed by lipid composition, mechanics, and lateral sorting. *PNAS Nexus* **4**, pgaf033 (2025).
63. L. Hogeveen, P. Boon, A. Mertens, L. Verhagen, K. Vonck, Therapeutic use of transcranial ultrasound for epilepsy: A review. *Heliyon* **11**, e43001 (2025).
64. S. Vanneste, J. Reynolds, D. De Ridder, Focused transcranial ultrasound stimulation: A breakthrough approach to treating brain disorders. *Expert Rev. Med. Devices* **22**, 1231–1242 (2025).
65. D. L. Miller *et al.*, Overview of therapeutic ultrasound applications and safety considerations. *J. Ultrasound Med.* **31**, 623–634 (2012).
66. S. Wu, J. Liu, Y. Tang, L. Yang, Y. Han, Skin burns after high-intensity focused ultrasound ablation: A retrospective control study. *Sci. Rep.* **15**, 28127 (2025).
67. Y. Meng, K. Hynynen, N. Lipsman, Applications of focused ultrasound in the brain: From thermoablation to drug delivery. *Nat. Rev. Neurol.* **17**, 7–22 (2021).
68. A. D. Bangham, R. W. Horne, Negative staining of phospholipids and their structural modification by surface-active agents as observed in the electron microscope. *J. Mol. Biol.* **8**, 660-IN10 (1964).
69. J. C. M. Stewart, Colorimetric determination of phospholipids with ammonium ferrothiocyanate. *Anal. Biochem.* **104**, 10–14 (1980).
70. M. J. Abraham *et al.*, GROMACS: High performance molecular simulations through multi-level parallelism from laptops to supercomputers. *SoftwareX* **1–2**, 19–25 (2015).
71. D. Van Der Spoel *et al.*, GROMACS: Fast, flexible, and free. *J. Comput. Chem.* **26**, 1701–1718 (2005).
72. P. C. T. Souza *et al.*, Martini 3: A general purpose force field for coarse-grained molecular dynamics. *Nat. Methods* **18**, 382–388 (2021).
73. T. A. Wassenaar, H. I. Ingólfsson, R. A. Böckmann, D. P. Tieleman, S. J. Marrink, Computational lipidomics with insaneâ€¯: A versatile tool for generating custom membranes for molecular simulations. *J. Chem. Theory Comput.* **11**, 2144–2155 (2015).
74. F. Grünewald *et al.*, Polyply; a python suite for facilitating simulations of macromolecules and nanomaterials. *Nat. Commun.* **13**, 68 (2022).
75. C. Brasnett, S. J. Marrink, MartiniGlass: A tool for enabling visualization of coarse-grained Martini topologies. *J. Chem. Inf. Model.* **65**, 3137–3141 (2025).
76. W. Humphrey, A. Dalke, K. Schulten, VMD: Visual molecular dynamics. *J. Mol. Graph.* **14**, 33–38 (1996).